ADVANCED FUNCTIONAL MATERIALS
www.afm-journal.de

Biomimetic Solar Photocatalytic Reactor for Selective Oxidation of Aromatic Alcohols with Enhanced Solar-Energy Utilization

Jingjing Qin, Jiahao Li, Kaibin Chu, Guozheng Yang, Leiqian Zhang, Xuemeng Xia, Pengyang Xuan, Xin Chen, Bo Weng, Haowei Huang, Yujie Chen, Wei Fan, YinBo Zhu, HengAn Wu, Feili Lai, and Tianxi Liu**

Low utilization of solar energy remains a challenge that limits photocatalytic efficiency. To address this issue, this work proposes a bionic solar photocatalytic reactor (BSPR) for efficient selective oxidation of aromatic alcohols. A biomimetic phototropic hydrogel is prepared by coupling chlorine-doped polypyrrole (Cl-PPy) and poly(*N*-isopropyl acrylamide) (PNIPAm) to maximize light-harvesting efficiency automatically, allowing the BSPR to maintain high catalytic levels throughout the day. Molecular dynamics simulations are used to unveil the understanding of the fast photoresponsive behavior of Cl-PPy/PNIPAm from a molecular level, while COMSOL simulations are conducted to follow the macroscopically phototropic mechanism of BSPR. Attributing to the existence of PdS/S vacancies riched $ZnIn_2S_4$ nanocomposite in the top flower-shaped hydrogel, the BSPR displays a special function for efficiently photocatalytic oxidation of aromatic alcohols under solar illumination (yield of 4-methoxybenzaldehyde: 479.5 μmol g^{-1} h^{-1}; selectivity: 68.8%). Two possible reaction pathways are identified as follows: photogenerated holes can attract aromatic alcohols directly and generate aromatic aldehydes; photoexcited electrons oxidize O_2 to $\cdot O_2^-$ can also react with the adsorbed aromatic alcohol. This study presents a promising paradigm that explores opportunities for enhanced utilization of light energy, offering a novel approach to maximize its efficiency in practical applications.

1. Introduction

The self-adaption abilities of biological systems in nature (e.g., mimosa pudica, sunflower, flytrap, etc.) are promoting the emergence of various smart materials,[1–4] that can change their structures, properties, and functions autonomously to respond to the innocuous stimuli (e.g., heat, pH, light, electricity, etc.) in their surrounding environments. In particular, light-responsive smart materials allow flexible manipulations at remote distances,[5–7] which are mainly driven by the intelligent composites of photothermal absorber and temperature-sensitive material for efficient photothermal conversion and thermally induced phase transition, respectively.[8–9] For the fabrication of these intelligent composites, the main task is to find suitable temperature-sensitive materials that can satisfy the requirements of diverse temperature ranges. Up to now, the most commonly used temperature-responsive materials include poly(*N*-isopropyl acrylamide) (PNIPAm), 2(dimethylamino)ethyl methacrylate, 4-(3-Acryloyloxypropyloxy)-benzoesure 2methyl-1,4-phenylester), and some other composites.[10–12] Among them, PNIPAm-based hydrogel can undergo a heat-induced conformational transition from a water-soluble coiled structure to a water-insoluble globular structure above its lower critical solubility temperature (LCST, ≈32 °C), resulting in the massive loss of confined water in the network of PNIPAm-based hydrogel with its notable volume reduction and

J. Qin, K. Chu, L. Zhang, X. Xia, P. Xuan, X. Chen, W. Fan, T. Liu
The Key Laboratory of Synthetic and Biological Colloids
Ministry of Education
School of Chemical and Material Engineering
International Joint Research Laboratory for Nano Energy Composites
Jiangnan University
Wuxi 214122, P. R. China
E-mail: txliu@jiangnan.edu.cn

J. Li, Y. Zhu, H. Wu
CAS Key Laboratory of Mechanical Behavior and Design of Materials
Department of Modern Mechanics
CAS Center for Excellence in Complex System Mechanics
University of Science and Technology of China
Hefei 230027, P. R. China

K. Chu, F. Lai
Department of Chemistry
KU Leuven
Celestijnenlaan 200F, Leuven 3001, Belgium
E-mail: feililai@sjtu.edu.cn

The ORCID identification number(s) for the author(s) of this article can be found under https://doi.org/10.1002/adfm.202311214

DOI: 10.1002/adfm.202311214

shape deformation.[13–16] Therefore, the photosensitive behaviors of PNIPAm-based hydrogel are closely related to the photothermal conversion efficiency/rate of the photothermal absorbers inside the PNIPAm-based hydrogel that can trigger the deswelling/swelling behavior of PNIPAm hydrogel by converting the absorbed light energy into thermal energy.[17] In this regard, abundant species of photothermal absorbers have been put forward, including graphene oxide, MXenes, polyaniline, and polypyrrole (PPy), and have been applied in the light-responsive smart materials (particularly in the PNIPAm-based hydrogels).[18–22] PPy stands out due to its strong near-infrared absorption, high photothermal property, and good photostability. Recently, Yu et al. demonstrated a rationally designed hybrid gel with an interpenetrating network formed by hydrophilic chloride-doped polypyrrole (Cl-PPy) and NIPAm,[23] which possesses a superior ability to release water upon illumination due to the presence of Cl-PPy nanoparticles. The interpenetrating network can also increase the gel/air interface area and act as a water channel during the water release process. However, hydrogel is still not suitable for light-driven applications due to its low cross-link density, which puts new requirements on the reasonable construction of light-responsive PNIPAm hydrogel with suitable structures.

The light-responsive smart materials can be used in various applications, such as drug delivery, tissue engineering, sensors, soft robotics, and artificial muscles, which makes them essential support for developing artificial smart systems.[24,25] In our recent works, we first put forward a new application of light-responsive smart materials as a photocatalytic reactor system (namely "biomimetic sunflower") inspired by sunflower that can capture sunlight spontaneously and utilize the light energy for photocatalysis maximumly.[26] However, this "biomimetic sunflower" is still suffering from the drawbacks of slow response to light and long recuperation time. c, reducing response time and recovery time are prerequisites for optimizing their solar energy utilization efficiency. By facilitating swift adjustments to the direction of sunlight and minimizing the required time for restoring the initial orientation, the biomimetic sunflower system can enhance its adaptability to changes in light, thereby effectively capturing sunlight and maintaining optimal performance. Therefore, it is urgent to develop a second-generation biomimetic photocatalytic system that can work under sunlight irradiation with high sensitivity to the change of light direction and quick shape recovery behavior, resulting in the full utilization of light energy.

G. Yang, Y. Chen, F. Lai
State Key Laboratory of Metal Matrix Composites
School of Materials Science and Engineering
Shanghai Jiao Tong University
Shanghai 200240, P. R. China
B. Weng, H. Huang
cMACS
Department of Microbial and Molecular Systems
KU Leuven
Celestijnenlaan 200F, Leuven 3001, Belgium
F. Lai
John A. Paulson School of Engineering and Applied Sciences
Harvard University
Cambridge, MA 02138, USA

As another main component in the biomimetic photocatalytic system, the photocatalyst itself determines the efficiencies directly for various photocatalytic reactions, such as the production of hydrogen peroxide, hydrogen evolution, selective oxidation of amine, and oxidation reaction of aromatic alcohol.[27–30] Among them, the photocatalytic oxidation reaction of aromatic alcohol to aromatic aldehyde is of great industrial significance, because aldehydes and their derivatives are essential building blocks for producing fine chemicals.[31] With the emergence of abundant efficient photocatalysts (e.g., metal oxides, metal sulfides, metal-free materials, etc.), the photocatalytic process can be realized under an economical and green condition.[32–35] To improve the light absorption characteristics and decrease transport pathways for photoexcited holes/electrons to the photocatalyst surface for efficient alcohol oxidation, the emergence of 2D semiconductors has opened up one effective approach owing to their unique properties of highly specific surface area, outstanding charge-carrier separation rate, and excellent conductivity.[36–39] $ZnIn_2S_4$ (ZIS) is a typical semiconductor that has received extensive attention in the field of photocatalysis due to its various morphologies (e.g., nanotube, nanosheet, and nanoflower), tunable bandgap (2.06–2.85 eV), and excellent photo-stability.[40,41] Nevertheless, the photocatalytic property of ZIS nanosheets is still confined by the rapid recombination of photo-excited charge carriers.[42,43] One of the most effective ways to overcome this obstacle is to introduce defect structures or co-catalysts in ZIS nanosheets.[44,45] Zhang et al. reported S vacancies (Vs), as electron traps, to prevent vertical transport of electrons and concentrate electrons near the Vs area, which are beneficial to enhancing the absorption of visible light and improving the photocatalytic activity significantly.[46] Additionally, the photocatalytic process may also be modulated by selecting suitable co-catalysts.[47] Based on previous studies, PdS is regarded as a suitable co-catalyst that can provide abundant active sites and improve electron transfer efficiency during the oxidation reaction.[48,49] However, the wide usage of PdS as a co-catalyst is still restricted by its poorly stable structure and easily agglomerated behavior, which is necessary to be solved by a suitable method for preparing stable PdS nanoparticles.

In this study, we developed a novel bionic solar photocatalytic reactor (BSPR) that can not only track the light automatically but also utilize solar energy maximally. To achieve the phototropic behavior of BSPR, Cl-PPy was incorporated with PNIPAm hydrogels that exhibited not only excellent photothermal conversion property but also phase transition capabilities. As a result, the phototropic hydrogel possessed high response and recovery rates, enabling maximum light capture at various irradiation angles. By introducing Vs into ZIS and depositing PdS nanoparticles, a highly effective nanocomposite photocatalyst was produced and incorporated at the top of BSPR. This resulted in improved separation of photogenerated electron–hole pairs, expanded light absorption spectra, and increased oxidation activity toward aromatic alcohols. This work demonstrates an effective way to make full use of solar catalysis.

2. Results and Discussion

Inspired by the sunflower in nature, we designed and fabricated a second-generation BSPR. As illustrated in **Figure 1**a, the BSPR consists of a hydrogel column and a flower-shaped hydrogel at

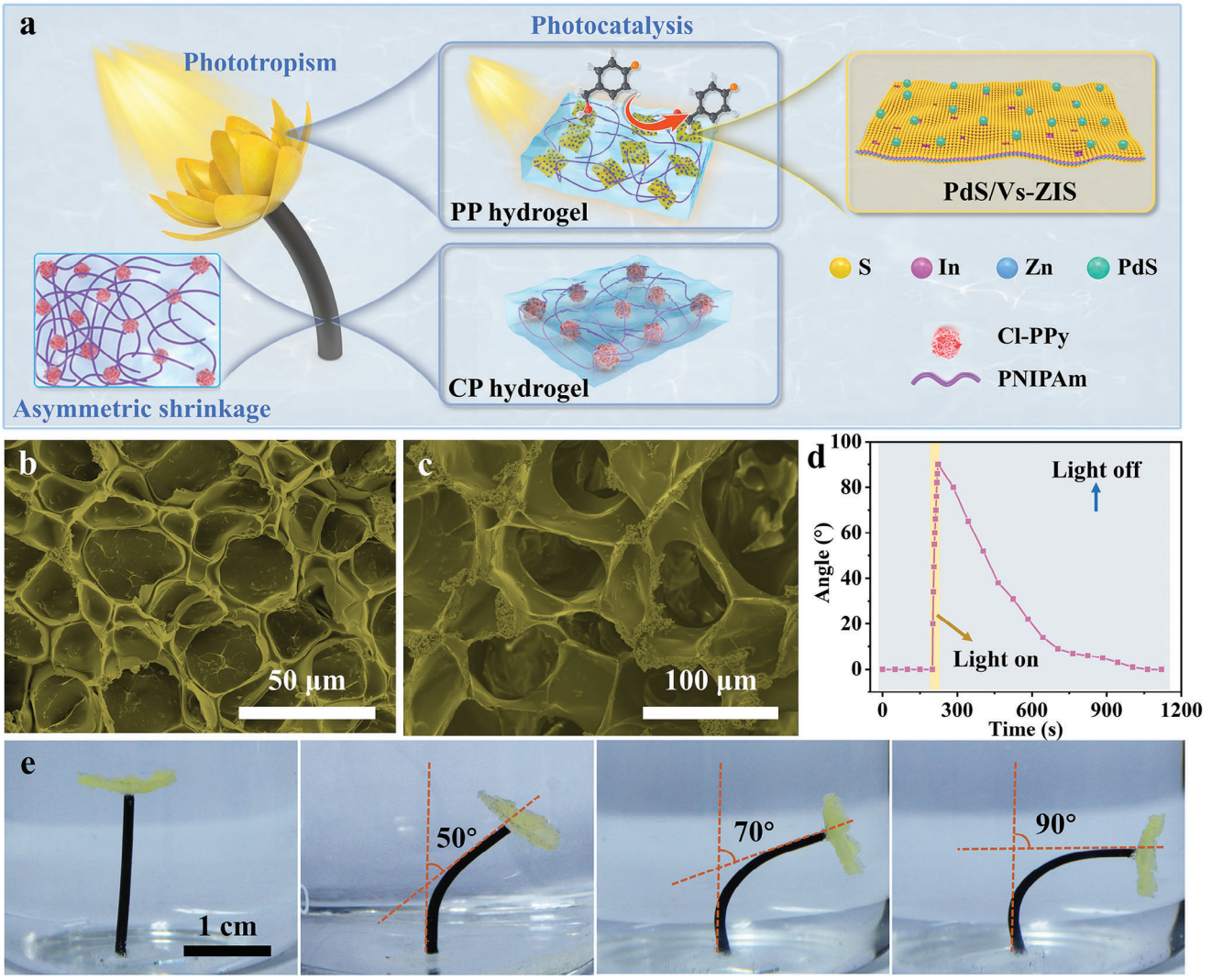

Figure 1. a) Schematic illustration for the preparation of BSPR. b,c) SEM images of the PP and CP hydrogel. d) The light-responsive behavior of the BSPR. e) Photographs of the BSPR at different zenith angles of incident light.

the bottom and top parts, respectively. In particular, the hydrogel column is composed of Cl-PPy and PNIPAm, which is phototropic due to the inhomogeneous deformation of the hydrogel column under illumination. Additionally, flower-shaped hydrogel is made up of PdS/Vs riched ZIS (PdS/Vs-ZIS) (vide infra) and PNIPAm. As the stress-strain curve of BSPR shown in Figure S1 (Supporting Information), a fracture strain value of 14.4% demonstrates the stable connection between Cl-PPy/PNIPAm (CP) hydrogel and PdS/Vs-ZIS/PNIPAm (PP) hydrogel. The phototropism enables the flower-shaped hydrogel perpendicular to the light source spontaneously, thereby maximizing sunlight absorption. The microstructures of the PP hydrogel and CP hydrogel were observed by scanning electron microscopy (SEM) technique. As depicted in Figure 1b, the PP hydrogel is composed of a 3D porous PNIPAm backbone without any observation of agglomerated PdS/Vs-ZIS nanosheets, indicating that the PdS/Vs-ZIS nanosheets are dispersed well inside the PP hydrogel. From the enlarged SEM image and corresponding energy dispersive spectroscopy (EDS) elemental mappings of PP hydrogel (Figure S2, Supporting Information), it can be observed that the PdS/Vs-ZIS nanosheets are embedded within the polymer framework uniformly to prevent the aggregation of PdS/Vs-ZIS nanosheets. As demonstrated in the SEM image of CP hydrogel (Figure 1c), the Cl-PPy nanoparticles (Figures S3 and S4, Supporting Information) are embedded into the pore walls of PNIPAm hydrogel. As the enlarged SEM image and corresponding EDS elemental mappings of CP hydrogel shown in Figure S5 (Supporting Information), the Cl-PPy nanoparticles are anchored on pore walls of the PNIPAm, indicating the successful preparation of CP hydrogel. This 3D framework of CP hydrogel is beneficial for the penetration of water into its internal space, which is essential for the realization of its photoresponsive behavior. Figure 1d and Figure S6 (Supporting Information) demonstrate that the BSPR displays reversible bending and recovering behaviors. The upright BSPR can bend to a 90° angle by 24 s irradiation. After turning off the light, the 90°-bent hydrogel column can return to its initial state

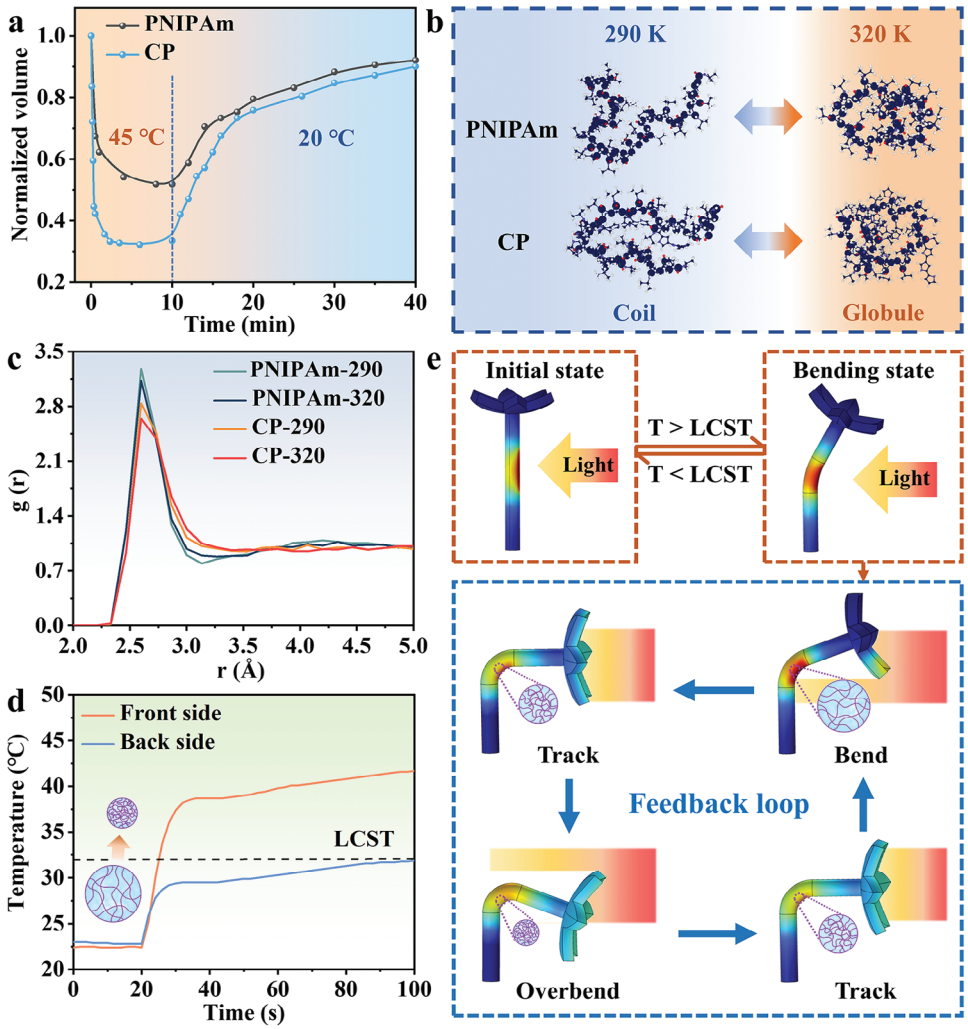

Figure 2. Phototropic mechanism of the BSPR. a) Thermal-stimulated volume shrinkage (at 45 °C) and recovery (at 20 °C) in water. b) Corresponding snapshots for the molecular structures of PNIPAm (top) and CP hydrogel (bottom) at 290 and 320 K. c) RDFs of C—H in PNIPAm and CP hydrogel obtained from the MD simulations under different temperatures. d) The time-dependent temperature at different sites of the BSPR. e) Schematic illustration for the phototropism mechanism of BSPR.

within 14 min. With more details displayed in Figure 1e, Figure S7 and Movie S1 (Supporting Information), the BSPR can separately adapt to the irradiations from various zenith angles (e.g., 50°, 70°, and 90°) and azimuth angles. These results indicate that BSPR has a wide response range, as well as a rapid response and recovery rate.

The phototropic behavior of the BSPR can be attributed to the inhomogeneous deformation caused by the locally high temperature of the BSPR induced by the effective photothermal process. As shown in Figure S8 (Supporting Information), a significant reduction in hydrogel volume occurs with the increase in external temperature. This is because the PNIPAm hydrogel undergoes the change from a hydrophilic state to a hydrophobic state when the ambient temperature exceeds its LCST (≈32 °C), leading to an obvious volume contraction. The presence of the Cl-PPy component enables the CP hydrogel to exhibit good photothermal conversion ability and results in a rapid photoresponsive function of PNIPAm hydrogel. Furthermore, the incorporation of Cl-PPy component will also affect the phase transition of hydrogel. As displayed in **Figure** 2a, the shrinkage and recovery rates for both PNIPAm and CP hydrogels are analyzed under different temperatures (45 and 20 °C). The CP hydrogel achieves an obvious shrinkage to 33% of its original size within 4 min at 45 °C, which can also return to its original volume quickly by immersing it in water at room temperature. However, the PNIPAm hydrogel only changes to 52% of its initial size with a longer time of 10 min as compared to that of CP hydrogel, indicating the introduction of Cl-PPy component in CP hydrogel can promote the shrinkage of the hydrogel. To further unveil this phenomenon, the phase transition processes of PNIPAm hydrogel and CP hydrogel were simulated by molecular dynamics (MD) calculations at 290 and 320 K, correspondingly. As illustrated in Figure 2b, both PNIPAm and CP hydrogel undergo conformation transition from coil states (290 K) to globule states (320 K) due to their hydrophilic to hydrophobic conversion. Meanwhile, the changes in hydrophobic interactions can also be quantified as the number

of contact between the C of PNIPAm chain and the H of water, provided by analyzing the radial distribution functions (RDFs) of PNIPAm chain in water at different temperatures (290 and 320 K).[23] The RDFs of C—H in Figure 2c show temperature dependences, where the intensities for the first peaks decrease gradually with the increase of temperature from 290 to 320 K (more details are shown in Table S1, Supporting Information). In particular, the height for the first peak of RDFs of the CP hydrogel at 320 K decreases by 0.20, which is larger than the decrease of PNIPAm (0.15), suggesting that the as-introduced Cl-PPy nanoparticles can promote the desolvation of PNIPAm. Other results also support this conclusion. Similarly, the conformational changes of the PNIPAm chain can also be quantified based on the number of contacts between the C atoms in the backbone and the C atoms of the CH_3 groups on the isopropyl side chain of PNIPAm. The results shown in Figure S9a (Supporting Information) also demonstrate temperature dependence in the RDFs between C atoms, with overall higher values at 320 K than those at 290 K. This is because, at higher temperatures, the chain mostly collapses, leading to more frequent contacts between C atoms than those at lower temperatures. In comparison to 290 K, the first peak of CP at 320 K increases by 205, which is higher than the increase of the first peak in PNIPAm from 290 to 320 K (68). Furthermore, by statistically analyzing the end-to-end distances of the chains, the changes in PNIPAm and CP chains can be further compared. As shown in Figure S9b (Supporting Information), the results indicate that the end-to-end distance of PNIPAm decreases by 11.0 Å at 320 K, while the CP chain decreases by 14.7 Å. The above results indicate that the addition of Cl-PPy can promote the collapse of PNIPAm chain, and lead to rapid photoresponse and recovery rate of BSPR. To understand the phototropism mechanism of BSPR better, the temperature variations at two sides of CP hydrogel were recorded using thermocouples under illumination. As shown in Figure 2d, the temperature on the front side of CP hydrogel rises to 38.2 °C within 12 s, whereas the temperature at the back side of CP hydrogel remains ≈29.5 °C (below the LCST). COMSOL Multiphysics simulation was carried out to simulate the temperature distributions for several critical states of the BSPR during the phototropic process. As shown in Figure 2e, the phototropic process of the BSPR is achieved by the built-in feedback loop with three typical steps of detecting, bending, and tracking processes (particularly, the tracking step is a dynamic balancing process). When the BSPR is illuminated with light from one side, the temperature on its irradiated side rises rapidly above the LCST (≈32 °C) of PNIPAm hydrogel due to the excellent photothermal conversion of Cl-PPy component, while the temperature on its back side still remains below the LCST. This simulation result corresponds well with the tested temperature variations in Figure 2d. Consequently, the network of CP hydrogel shrinks asymmetrically and results in the quick bend of BSPR toward the light. Once the BSPR has overbent, it experiences a self-shadowing state that results in decreased temperature on the front side ultimately. This triggers a natural hydrogel recovery mechanism, leading to automatic repetition of the cycle.

Phototropism is an essential prerequisite for BSPR to capture sunlight continuously and enable efficient conversion of light energy. The photocatalytic ability of BSPR is mainly determined by the photocatalyst incorporated in the flower-shaped hydrogel (PP hydrogel), which was obtained by introducing Vs and depositing PdS nanoparticles on ZIS nanosheets toward photocatalytic oxidization of aromatic alcohols. The crystal structures of the as-prepared ZIS and Vs-ZIS nanosheets were analyzed by using X-ray diffraction (XRD) method. The diffraction peaks for both ZIS and Vs-ZIS nanosheets observed in Figure S10 (Supporting Information) are in good agreement with a hexagonal structure of ZIS (JCPDS No. 72–0773). These diffraction peaks are located at 21.4°, 27.9°, 30.7°, 39.5°, 47.4°, 52.3° and 55.8°, corresponding to (006), (102), (104), (108), (110), (116), and (202), respectively.[50] The transmission electron microscopy (TEM) image of the obtained Vs-ZIS nanosheets shown in Figure S11 (Supporting Information), consists of abundant ultrathin nanosheets. The specific thicknesses of ZIS and Vs-ZIS nanosheets are ≈1.82 and 1.60 nm, respectively, from their atomic force microscopy (AFM) images (Figure S12, Supporting Information), indicating the presence of Vs would reduce the thickness of the ZIS nanosheets. After loading slight PdS nanoparticles on the surface of Vs-ZIS nanosheets via the photodeposition method, the Vs-ZIS nanosheets are decorated with abundant ultrafine PdS nanoparticles (nanoparticle size of ≈10 nm) uniformly, leading to the generation of PdS-1/Vs-ZIS ("1" indicates the added amount of Pd is 1 wt. % of the weight of Vs-ZIS) nanocomposite (**Figure** 3a). The EDS elemental mappings of the PdS-1/Vs-ZIS (Figure 3b) show that the elements of Zn, In, and S are distributed in PdS-1/Vs-ZIS nanocomposite homogeneously. Meanwhile, Figure 3b further confirms that the main element composition of the nanoparticle on the Vs-ZIS nanosheets is predominantly Pd. The X-ray photoelectron spectroscopy (XPS) spectrum of Pd 3d in PdS-1/Vs-ZIS is shown in Figure S13 (Supporting Information). The binding energies of Pd $3d_{5/2}$ and Pd $3d_{3/2}$ are 337.0 and 342.2 eV, respectively, which are consistent with the characteristics of Pd^{2+}. Additionally, the high-resolution transmission electron microscopy (HRTEM) image of PdS-1/Vs-ZIS nanocomposite presented in Figure 3c illustrates clear lattice fringes of 0.32 and 0.23 nm, which belong to (102) plane of ZIS and (202) plane of PdS,[36,47] respectively. To be noted, no characteristic diffraction peaks for PdS phase can be observed in the XRD pattern of PdS-1/Vs-ZIS (Figure S10, Supporting Information), which is ownned to the low loading amount and homogeneous dispersion of ultrafine PdS nanoparticles in the Vs-ZIS nanosheets. The above-mentioned results collectively confirm the successful loading of PdS nanoparticles on the surface of Vs-ZIS nanosheets.

Moreover, electron paramagnetic resonance (EPR), inductively coupled plasma mass spectrometry (ICP-MS), and XPS methods were carried out to confirm the existence of Vs in Vs-ZIS nanosheets. As shown in Figure 3d, the Vs-ZIS exhibits a much sharper EPR signal at a *g*-value of 2.003 than that of ZIS, which indicates the existence of abundant vacancies in Vs-ZIS nanosheets. From the ICP-MS results in Table S2 (Supporting Information), the atomic ratios of Zn, In, and S in ZIS and Vs-ZIS nanosheets are 1:2.2:3.7 and 1:2.3:2.8, respectively, demonstrating that the Vs-ZIS contains abundant Vs instead of Zn vacancies. XPS spectra are obtained to analyze chemical compositions and chemical states. As compared to ZIS, the binding energy values of S 2p peaks (S $2p_{1/2}$ and S $2p_{3/2}$) in Vs-ZIS shift negatively, as shown in Figure S14 (Supporting Information). In particular, the binding energy values of S 2p in Vs-ZIS (163.00 and 161.85 eV) are lower than those in ZIS (163.18 and 162.01 eV), which is due

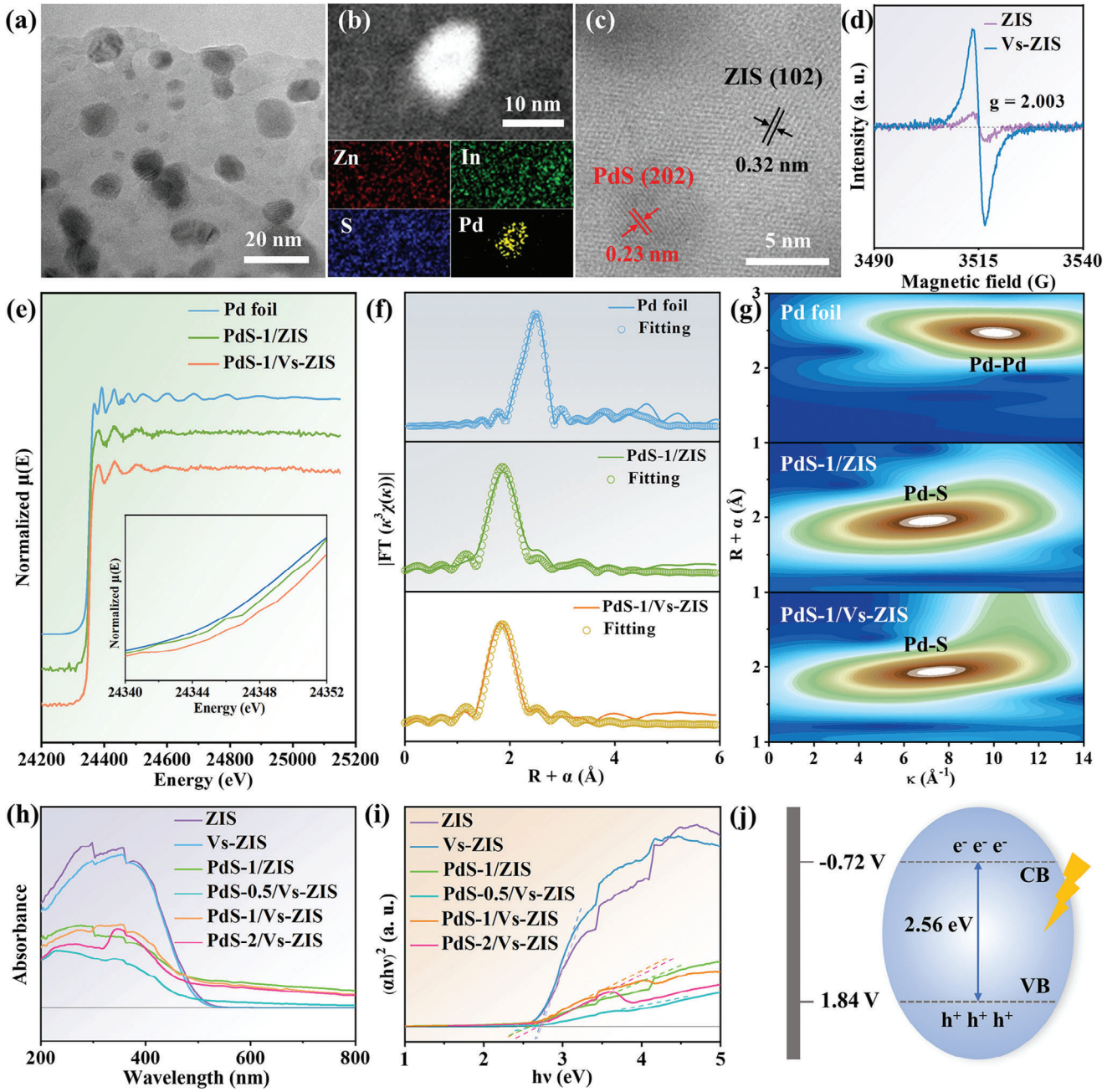

Figure 3. a) TEM image, b) HAADF-STEM image and corresponding EDS elemental mappings, and c) HRTEM image of PdS-1/Vs-ZIS nanocomposite. d) EPR spectra of ZIS and Vs-ZIS nanosheets. e) Pd K-edge XANES profiles of Pd foil, PdS-1/ZIS, and PdS-1/Vs-ZIS. The inset in (e) shows the magnified near-edge structures of different catalysts. f) FT-EXAFS spectra of Pd K-edge and g) Wavelet transform of EXAFS spectra at Pd K-edge for Pd foil, PdS-1/ZIS, and PdS-1/Vs-ZIS. h) UV–vis absorption spectra and i) bandgap energies of ZIS, Vs-ZIS, PdS-1/ZIS, PdS-0.5/Vs-ZIS, PdS-1/Vs-ZIS, and PdS-2/Vs-ZIS. j) Band diagram of the PdS-1/Vs-ZIS photocatalyst.

to the low-coordinated S element in Vs-ZIS. The above results indicate that an excess of thioacetamide can lead to the generation of abundant Vs on ZIS nanosheets. This is because the excessive thioacetamide can adsorb on the surface of the primary nanocrystals to hinder the growth of the crystals partially and result in the formation of a Vs-rich structure.[50,51] To investigate the coordination structure of the Pd atom, X-ray absorption near-edge structure (XANES) spectroscopy was recorded. As shown in Figure 3e, the absorption edge of PdS-1/Vs-ZIS shifts positively based on the curve of PdS-1/ZIS, demonstrating that the valence state of Pd in PdS-1/Vs-ZIS is higher than PdS-1/ZIS. Fourier-transformed X-ray absorption fine structure (FT-EXAFS) spectra and corresponding fitting parameters at the Pd K-edge for various samples are displayed in Figure 3f and Table S3 (Supporting Information), respectively. The Pd—S bonds with lengths of 1.87 and 1.84 Å and coordination numbers of 2.35 and 2.53 can be

observed in the PdS-1/ZIS and PdS-1/Vs-ZIS nanocomposites, respectively. The presence of Vs in Vs-ZIS nanosheets would lead to a reduced Pd—S bond length and an increased coordination number in PdS-1/Vs-ZIS on account of the redistributed charges around the Vs. The wavelet transforms (WT) of EXAFS spectra of PdS-1/ZIS and PdS-1/Vs-ZIS (Figure 3g) show the maximum values of PdS-1/ZIS and PdS-1/Vs-ZIS locate at 7.1 and 7.5 $Å^{-1}$ in the k space, respectively, which correspond to the Pd—S bonds.[52] These values are completely different from that of the Pd foil at 10.1 $Å^{-1}$. To go further, ultraviolet–visible diffuse reflectance spectra (UV–Vis DRS) were employed to explore the optical absorption characteristics of ZIS, Vs-ZIS, PdS-1/ZIS, PdS-0.5/Vs-ZIS, PdS-1/Vs-ZIS, and PdS-2/Vs-ZIS. As illustrated in Figure 3h,i, the ZIS has an absorption edge at ≈454 nm, whereas the PdS-1/Vs-ZIS exhibits a stronger visible light absorption edge at 484 nm. Based on Tauc plots, the calculated bandgap energies for ZIS, Vs-ZIS, PdS-1/ZIS, PdS-0.5/Vs-ZIS, PdS-1/ZIS and PdS-2/Vs-ZIS are 2.73, 2.71, 2.57, 2.65, 2.56, and 2.66 eV, respectively, indicating that PdS-1/Vs-ZIS has the most excellent absorption capability of visible light.

Furthermore, the flat-band potentials (E_{FB}) of ZIS, Vs-ZIS, PdS-1/ZIS, PdS-0.5/Vs-ZIS, PdS-1/Vs-ZIS, and PdS-2/Vs-ZIS were determined using Mott–Schottky measurement. Figure S15 (Supporting Information) shows the positive slopes of the obtained curves are consistent with those of typical n-type semiconductors.[33] Based on the above-measured results in Figure 3h and Figure S15 (Supporting Information), therefore, the band structures of ZIS, Vs-ZIS, PdS-1/ZIS, PdS-0.5/Vs-ZIS, PdS-1/Vs-ZIS, and PdS-2/Vs-ZIS can be evaluated and summarized in Table S4 (Supporting Information). The E_{FB} values of the ZIS, Vs-ZIS, PdS-1/ZIS, PdS-0.5/Vs-ZIS, PdS-1/Vs-ZIS, and PdS-2/Vs-ZIS are measured to be −0.47, −0.49, −0.67, −0.71, −0.82, and −0.86 V (vs Ag/AgCl), respectively. Based on these values, the conduction band (CB) positions of ZIS, Vs-ZIS, PdS-1/ZIS, PdS-0.5/Vs-ZIS, PdS-1/Vs-ZIS, and PdS-2/Vs-ZIS are estimated to be −0.37, −0.39, −0.57, −0.61, −0.72, and −0.76 V, respectively. The band structure of the PdS-1/Vs-ZIS photocatalyst is shown in Figure 3j. To further reveal the impact of Vs and introduced PdS nanoparticles on charge separation and transfer, steady-state photoluminescence (PL) spectra are employed in Figure S16 (Supporting Information). As the broad peak at 450 nm results from the photo-generated electron–hole recombination, the lower peak intensity of Vs-ZIS than that of ZIS verifies the satisfied charge separation of Vs-ZIS. In addition, an appropriate amount of existing PdS nanoparticles can further reduce the intensity of the emission peak. When an excess amount of PdS nanoparticles is loaded, however, the intensity of the emission peak increases slightly, indicating that an excess of PdS would promote the recombination of photo-generated electron–hole pairs.

To further evaluate the photocatalytic activity of various samples (ZIS, Vs-ZIS, PdS-1/ZIS, PdS-0.5/Vs-ZIS, PdS-1/Vs-ZIS, and PdS-2/Vs-ZIS), the photocatalytic oxidation of 4-methoxybenzyl alcohol (4-MBA) was carried out as an example under xenon lamp (300 W) irradiation for 4 h. As shown in **Figure** 4a, the Vs-ZIS exhibits a higher yield of 4-methoxybenzaldehyde (4-MBAL) (176.7 μmol g^{-1} h^{-1}) than that of pristine ZIS (90.0 μmol g^{-1} h^{-1}). When PdS nanoparticles were loaded on ZIS nanosheets, the yield of PdS/ZIS was 5.4 times that of pristine ZIS. In addition, with the dopant of PdS nanoparticles, the production rates of 4-MBAL over PdS/Vs-ZIS display significantly increasing trends. In particular, among various PdS/Vs-ZIS nanosheets with different PdS contents, the PdS-1/Vs-ZIS possesses not only the highest 4-MBAL yield of 484.2 μmol g^{-1} h^{-1}, but also the highest selectivity of 68.6% Besides, the main by-product from the photocatalytic oxidation of 4-MBA is detected as 4-methoxybenzoic acid with a selectivity of 30.5% (Table S5, Supporting Information). Nevertheless, an excessive amount of PdS in PdS/Vs-ZIS leads to a decline in performance. For instance, in the case of PdS-2/Vs-ZIS, the selective photocatalytic oxidation of 4-MBA to 4-MBAL results in a reduced yield of 320.2 μmol g^{-1} h^{-1} and a decreased selectivity of 53.1%. There are two reasons for the reduction in the photocatalytic performance of PdS-2/Vs-ZIS. On the one hand, it can be observed that an excess of PdS nanoparticles hinders the separation of photo-generated charge-carrier pairs from the PL spectra (Figure S16, Supporting Information), thereby reducing the photocatalytic performance. On the other hand, an excess of PdS agglomerates on the Vs-ZIS nanosheets (Figure S17, Supporting Information), further reduced the number of activity sites for the oxidation reaction. Furthermore, other aromatic alcohols of 4-nitrobenzyl alcohol (4-NBA), 4-chlorobenzyl alcohol (4-CBA), and benzyl alcohol (BA) were also employed as reactants to check the selective photocatalytic oxidation properties of various catalysts. The results indicate that PdS-1/Vs-ZIS exhibits the best photocatalytic performance in terms of yield and selectivity. As shown in Figure S18 (Supporting Information), the PdS-1/Vs-ZIS can maintain an impressive 91.2% of its initial activity after seven successive reaction cycles, demonstrating its excellent recycling stability for potential practical application. The results in Table S6 (Supporting Information) indicate that the catalytic performance of Pds-1/Vs-ZIS ranks at a moderately high level.

Subsequently, PdS-1/Vs-ZIS was utilized as a photocatalyst in BSPR to evaluate its autonomous light-harvesting ability of BSPR. The UV–vis absorption spectrum of PP hydrogel in Figure S19 (Supporting Information) and PdS-1/Vs-ZIS in Figure 3h exhibit similar absorption band structures, indicating that the integration of PdS-1/Vs-ZIS and PNIPAm cannot affect the effective absorption and utilization of light energy by PdS-1/Vs-ZIS. Thanks to the 3D porous structure of the hydrogel, solute molecules can diffuse and transport through the interconnected pores and channels of the hydrogel efficiently, enabling effective interaction between PdS-1/Vs-ZIS and reactants. Building upon this, some BSPRs form adaptive photocatalytic systems that allow for the maximum harvesting of solar energy. As shown in Figure 4e and Movie S2 (Supporting Information), the yields for photocatalytic oxidation of 4-MBA to 4-MBAL are examined at different irradiation angles. To be noted, the 3D porous structure for the PP hydrogel (Figure 1b) is beneficial to facilitating mass transport through abundant channels and the adsorption of reactant during photocatalysis. As the angle of incidence increases from 0° to 90°, the yield for 4-MBAL production decreases from 486.5 to 159.5 μmol g^{-1} h^{-1} in the control sample (the photocatalytic reactor without phototropic ability). However, the photocatalytic activity of the BSPRs can still remain at a high level. At 0° incidence angle, the photocatalytic oxidation of 4-MBA achieves a yield of 479.5 μmol g^{-1} h^{-1} with a selectivity of 68.8%. Meanwhile, at 90° incidence angle, the yield and selectivity are reduced

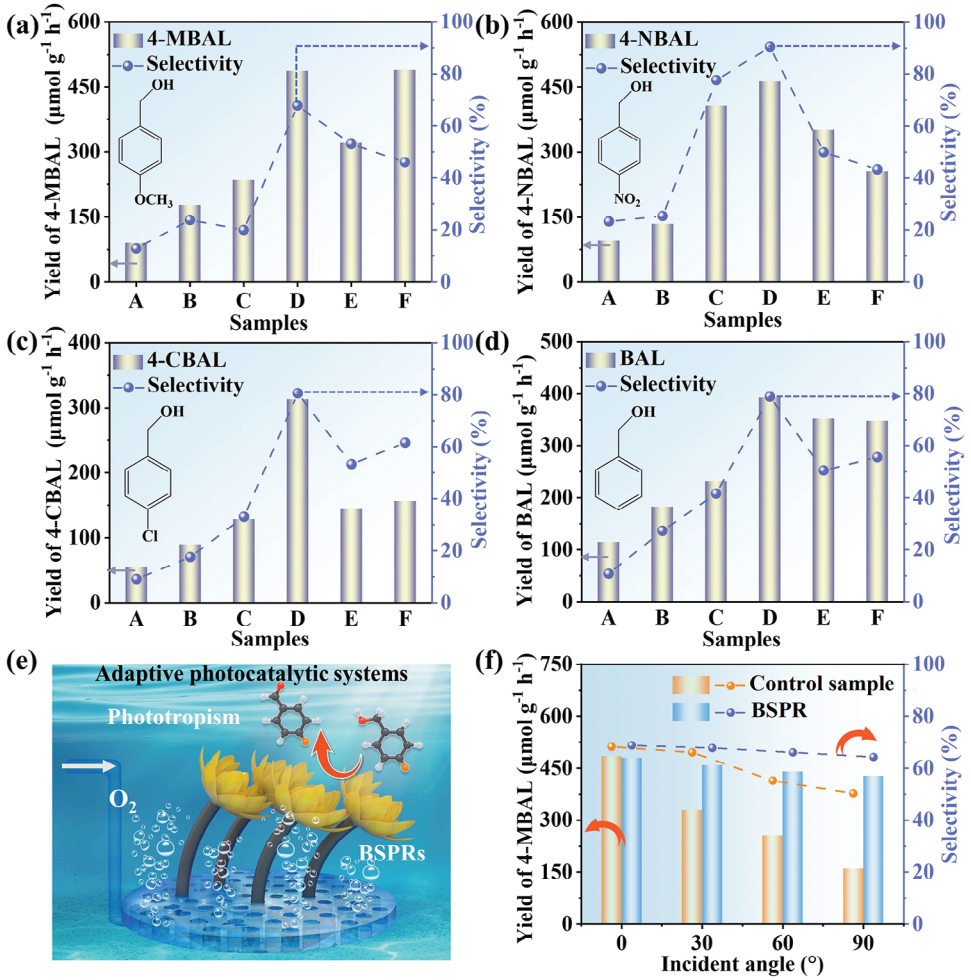

Figure 4. Photocatalytic oxidation of a) 4-MBA, b) 4-NBA, c) 4-CBA, and d) BA over different catalysts with a reaction time of 4 h. Here, A, B, C, D, E, and F represent ZIS, Vs-ZIS, PdS-0.5/Vs-ZIS, PdS-1/Vs-ZIS, PdS-2/Vs-ZIS, and PdS-1/ZIS, respectively. e) Schematic diagram of an adaptive photocatalytic system for photocatalytic oxidation of aromatic alcohol. f) The yield for the photocatalytic 4-MBAL production of BSPR and control sample at different incident angles.

to 427.1 μmol g^{-1} h^{-1} and 64.3%, respectively. These results indicate that the phototropic behavior of the BSPRs is beneficial for light-harvesting to achieve maximum light utilization toward the photocatalytic process.

To reveal the reaction mechanism, the potential active species that are responsible for aromatic alcohol conversion were analyzed by a series of controlled experiments, where carbon tetrachloride (CCl_4), methanol (CH_3OH), isopropyl (IPA), and 1,4-benzoquinone (BQ) were used as scavengers to trap the photogenerated electron (e^-), hole (h^+), hydroxyl radical (·OH), and superoxide radical ($\cdot O_2^-$), respectively. As displayed in **Figure 5a**, the addition of CH_3OH and BQ would lead to the reduced photocatalytic yields of 4-MBAL to 275.2 and 163.0 μmol g^{-1} h^{-1}, respectively, which confirm that the photogenerated holes and $\cdot O_2^-$ can act as the active centers and participate in the photocatalytic reaction. The addition of IPA shows a negligible influence on the production of 4-MBAL and demonstrates the weak role of ·OH in photocatalysis. Remarkably, the introduction of the CCl_4 scavenger would still result in a high yield of 4-MBAL, indicating the direct oxidation of 4-MBA to 4-MBAL by photoexcited holes. Furthermore, the utilization of CCl_4 as an electron scavenger in the reaction system impeded the formation of $\cdot O_2^-$, while still achieving a higher yield compared to utilizing BQ as an $\cdot O_2^-$ trapping agent. This can be attributed to the prevented recombination of photogenerated electrons and holes by the addition of CCl4, leading to an increased efficiency of the photoexcited holes for photocatalysis.[53] The EPR technique was further applied to discriminate the transient radical species. 5, 5-dimethyl-1-pyrroline-N-oxide (DMPO) was used to detect the $\cdot O_2^-$ radical and carbon-centered radical with CH_3OH and N_2-saturated water as solvents, respectively. As shown in Figure 5b, the EPR signal of $\cdot O_2^-$ can be well observed in the presence of DMPO and proves the generation of $\cdot O_2^-$ upon photoexcitation of PdS-1/Vs-ZIS in the system, which is due to the well-matched standard potential of $O_2/\cdot O_2^-$ (−0.33 eV vs NHE)[32] and CB of PdS-1/Vs-ZIS (Table S4, Supporting Information). It is noted, that no apparent EPR signal is detected in the dark, suggesting that the formation of radical species is closely dependent on light exposure. Besides, it is theoretically possible to produce singlet oxygen ($^1O_2$) during the reaction. However, no signal of singlet oxygen (Figure 5c)

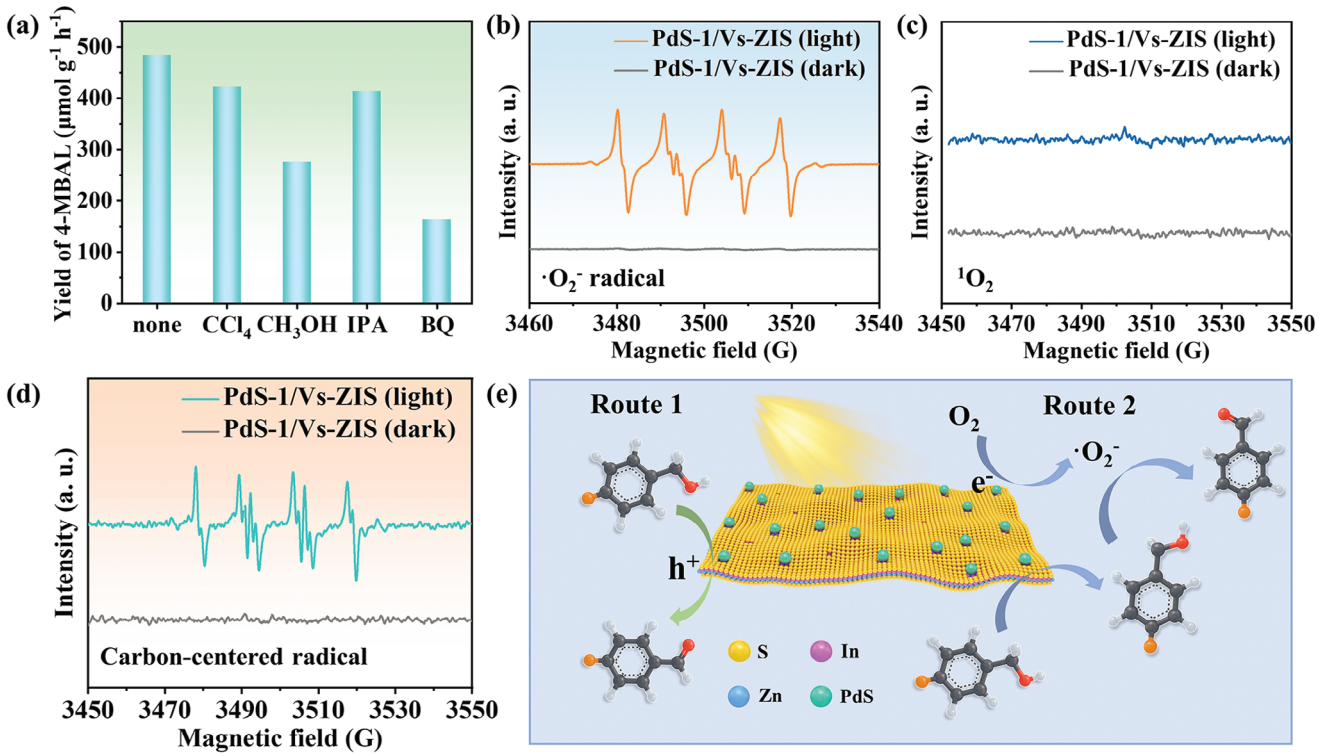

Figure 5. a) The photocatalytic conversion of 4-MBA over PdS-1/Vs-ZIS by adding different scavengers. EPR detections of formed b) DMPO-$\cdot O_2^-$, c) TMP-$^1O_2$, and d) carbon-centered radical for PdS-1/Vs-ZIS under dark and light irradiation. e) The proposed reaction mechanism for photocatalytic selective oxidation of aromatic alcohol to aromatic aldehyde.

can be detected in both dark and light conditions, indicating its absence in the reaction. These results demonstrate that $\cdot O_2^-$ is the main radical species for photocatalytic oxidation. Moreover, carbon-centered radicals produced in the process of 4-MBA oxidation can also be detected under light (Figure 5d), indicating that carbon-centered radical is an intermediate for the 4-MBA transformation in the photocatalytic process. Thus, a possible reaction mechanism for the photocatalytic oxidation of aromatic alcohols has been proposed in Figure 5e, which consists of two pathways: i) photo-generated holes can attract aromatic alcohols directly and generate aromatic aldehydes; ii) rapid oxidation of O_2 to $\cdot O_2^-$ occurs via photoexcited electrons that can react with the adsorbed alcohol radical cation (activated by the generated holes) on the catalyst surface to produce 4-MBAL.

3. Conclusion

A BSPR system was developed to enhance the efficiency of photocatalytic oxidation of aromatic alcohols by optimizing light-harvesting and modulating the electronic structures of photocatalysts. The bottom of the BSPR features a PNIPAm hydrogel column incorporated with Cl-PPy, enabling fast and adaptive phototropic behavior. Molecular dynamics simulations were employed to analyze the conformational transition of hydrogel molecules, as well as the role of Cl-PPy in facilitating the deformation and shape recovery process of the hydrogel column. COMSOL calculations were also conducted to elucidate the photoinduction mechanism and heat distribution in different stages of the phototropism process. Additionally, the introduction of PdS nanoparticles and Vs enhanced the photocatalytic oxidation efficiency of aromatic alcohols by improving charge carrier separation and expanding the absorption of PdS/Vs-ZIS nanocomposite. Furthermore, the incorporation of PdS-1/Vs-ZIS into the flower-shaped hydrogel atop the BSPR demonstrated efficient catalytic activity in the transformation of aromatic alcohols into aromatic aldehydes. The results demonstrate the consistently high catalytic efficiency of the BSPR at different zenith angles, providing a novel approach for utilizing light energy in catalysis.

Supporting Information

Supporting Information is available from the Wiley Online Library or from the author.

Acknowledgements

The authors are grateful for the financial support from the National Natural Science Foundation of China (52303151), the Research Foundation Flanders (1298323N and V404923N), the Shanghai Scientific and Technological Innovation Project (18JC1410600), the Program of the Shanghai Academic Research Leader (17XD1400100), the National Key Research and Development Program of China (2022YFB3805700), the Postgraduate Research & Practice Innovation Program of Jiangsu Province (nos. KYCX23_2456), and the Fundamental Research Funds for the Central Universities. The authors thank the BL14W1 station in Shanghai Synchrotron Radiation Facility (SSRF) for the help in characterizations. The authors also thank the characterizations supported by Central Laboratory, School of Chemical and Material Engineering, Jiangnan University.

Conflict of Interest

The authors declare no conflict of interest.

Data Availability Statement

The data that support the findings of this study are available from the corresponding author upon reasonable request.

Keywords

oxidation of aromatic alcohols, photocatalysis, PNIPAm, smart hydrogels

Received: September 15, 2023
Revised: October 28, 2023
Published online: November 17, 2023

[1] H. Sun, Y. He, Z. Wang, Q. Liang, *Adv. Funct. Mater.* **2022**, *32*, 2108489.
[2] W. Wang, P.-F. Li, R. Xie, X.-J. Ju, Z. Liu, L.-Y. Chu, *Adv. Mater.* **2022**, *34*, 2107877.
[3] X. Lv, J. Mao, S. Yang, H. Zhang, J. Chen, F. Luo, *Comp. Commun.* **2023**, *42*, 101670.
[4] P. Lavrador, M. R. Esteves, V. M. Gaspar, J. F. Mano, *Adv. Funct. Mater.* **2021**, *31*, 2005941.
[5] Q. L. Zhu, C. Du, Y. Dai, M. Daab, M. Matejdes, J. Breu, W. Hong, Q. Zheng, Z. L. Wu, *Nat. Commun.* **2020**, *11*, 5166.
[6] Q. L. Zhu, C. F. Dai, D. Wagner, M. Daab, W. Hong, J. Breu, Q. Zheng, Z. L. Wu, *Adv. Mater.* **2020**, *32*, 2005567.
[7] L. Li, J. M. Scheiger, P. A. Levkin, *Adv. Mater.* **2019**, *31*, 1807333.
[8] Q. L. Zhu, C. F. Dai, D. Wagner, O. Khoruzhenko, W. Hong, J. Breu, Q. Zheng, Z. L. Wu, *Adv. Sci.* **2021**, *8*, 2102353.
[9] F. Li, X. Sun, J. Yang, J. Ren, M. Huang, S. Wang, D. Yang, *Adv. Sci.* **2023**, *10*, 2204905.
[10] W. Li, T. Kuang, X. Jiang, J. Yang, P. Fan, Z. Zhao, Z. Fei, M. Zhong, L. Chang, F. Chen, *Chem. Eng. J.* **2017**, *322*, 445.
[11] Z. Chen, Y. Chen, Y. Guo, Z. Yang, H. Li, H. Liu, *Adv. Funct. Mater.* **2022**, *32*, 2201009.
[12] Y. Zhang, Z. Wang, Y. Yang, Q. Chen, X. Qian, Y. Wu, H. Liang, Y. Xu, Y. Wei, Y. Ji, *Sci. Adv.* **2020**, *6*, eaay8606.
[13] A. K. Mishra, T. J. Wallin, W. Pan, P. Xu, K. Wang, E. P. Giannelis, B. Mazzolai, R. F. Shepherd, *Sci. Robot.* **2020**, *5*, eaaz3918.
[14] Z. Li, L. Liu, H. Zheng, F. Meng, F. Wang, *Comp. Commun.* **2022**, *35*, 101327.
[15] S. Li, H. Yang, N. Zhu, G. Chen, Y. Miao, J. Zheng, Y. Cong, Y. Chen, J. Gao, X. Jian, J. Fu, *Adv. Funct. Mater.* **2022**, *33*, 2211189.
[16] a) J. Zhu, M. Yao, S. Huang, J. Tian, Z. Niu, *Angew. Chem., Int. Ed.* **2020**, *59*, 16480; b) J. Zhu, M. Yao, S. Huang, J. Tian, Z. Niu, *Angew. Chem.* **2020**, *132*, 16622.
[17] H. Zhao, Y. Huang, F. Lv, L. Liu, Q. Gu, S. Wang, *Adv. Funct. Mater.* **2021**, *31*, 2105544.
[18] Z. Zhao, H. Wang, L. Shang, Y. Yu, F. Fu, Y. Zhao, Z. Gu, *Adv. Mater.* **2017**, *29*, 1704569.
[19] Y. Zhao, C.-Y. Lo, L. Ruan, C.-H. Pi, C. Kim, Y. Alsaid, I. Frenkel, R. Rico, T.-C. Tsao, X. He, *Sci. Robot.* **2021**, *6*, eabd5483.
[20] C.-Y. Lo, Y. Zhao, C. Kim, Y. Alsaid, R. Khodambashi, M. Peet, R. Fisher, H. Marvi, S. Berman, D. Aukes, X. He, *Mater. Today Bio.* **2021**, *50*, 35.
[21] H. Bai, T. Fan, H. Guan, Y. Su, J. Zhang, J. Wang, S. Ramakrishna, Y.-Z. Long, *Compos. Commun.* **2022**, *31*, 101104.
[22] J. Han, W. Xing, J. Yan, J. Wen, Y. Liu, Y. Wang, Z. Wu, L. Tang, J. Gao, *Adv. Fiber Mater.* **2022**, *4*, 1233.
[23] F. Zhao, X. Zhou, Y. Liu, Y. Shi, Y. Dai, G. Yu, *Adv. Mater.* **2019**, *31*, 1806446.
[24] P. Theato, B. S. Sumerlin, R. K. O'Reilly, T. H. Epps, Iii, *Chem. Soc. Rev.* **2013**, *42*, 7055.
[25] M. Wei, Y. Gao, X. Li, M. J. Serpe, *Polym. Chem.* **2017**, *8*, 127.
[26] J. Qin, K. Chu, Y. Huang, X. Zhu, J. Hofkens, G. He, I. P. Parkin, F. Lai, T. Liu, *Energy Environ. Sci.* **2021**, *14*, 3931.
[27] J. Wan, L. Liu, Y. Wu, J. Song, J. Liu, R. Song, J. Low, X. Chen, J. Wang, F. Fu, Y. Xiong, *Adv. Funct. Mater.* **2022**, *32*, 2203252.
[28] H. Zhang, Q. Li, B. Weng, L. Xiao, Z. Tian, J. Yang, T. Liu, F. Lai, *Chem. Eng. J.* **2022**, *442*, 136144.
[29] H. Chen, L. Peng, Y. Bian, X. Shen, J. Li, H.-C. Yao, S.-Q. Zang, Z. Li, *Appl. Catal., B* **2021**, *284*, 119704.
[30] F. Xing, R. Zeng, C. Cheng, Q. Liu, C. Huang, *Appl. Catal., B* **2022**, *306*, 121087.
[31] M. Bellardita, E. I. García-López, G. Marcì, I. Krivtsov, J. R. García, L. Palmisano, *Appl. Catal., B* **2018**, *220*, 222.
[32] C. Jiang, H. Wang, Y. Wang, H. Ji, *Appl. Catal., B* **2020**, *277*, 119235.
[33] a) Z. Zhu, H. Huang, L. Liu, F. Chen, N. Tian, Y. Zhang, H. Yu, *Angew. Chem., Int. Ed.* **2022**, *61*, e202203519; b) Z. Zhu, H. Huang, L. Liu, F. Chen, N. Tian, Y. Zhang, H. Yu, *Angew. Chem.* **2022**, *134*, e202203519.
[34] W. Shang, Y. Li, H. Huang, F. Lai, M. B. J. Roeffaers, B. Weng, *ACS Catal.* **2021**, *11*, 4613.
[35] X. Sun, L. Li, S. Jin, W. Shao, H. Wang, X. Zhang, Y. Xie, *eScience* **2023**, *3*, 100095.
[36] Y. Peng, M. Geng, J. Yu, Y. Zhang, F. Tian, Y.a' Guo, D. Zhang, X. Yang, Z. Li, Z. Li, S. Zhang, *Appl. Catal., B* **2021**, *298*, 120570.
[37] H. Zhang, Q. Li, B. Li, B. Weng, Z. Tian, J. Yang, J. Hofkens, F. Lai, T. Liu, *J. Catal.* **2022**, *407*, 1.
[38] X. Zhu, L. Mo, Y. Wu, F. Lai, X. Han, X. Y. Ling, T. Liu, Y.-E. Miao, *Compos. Commun.* **2018**, *9*, 86.
[39] W. Zong, C. Yang, L. Mo, Y. Ouyang, H. Guo, L. Ge, Y.-E. Miao, D. Rao, J. Zhang, F. Lai, T. Liu, *Nano Energy* **2020**, *77*, 105189.
[40] H. Fan, Y. Jin, K. Liu, W. Liu, *Adv. Sci.* **2022**, *9*, 2104579.
[41] P. Jin, L. Wang, X. Ma, R. Lian, J. Huang, H. She, M. Zhang, Q. Wang, *Appl. Catal., B* **2021**, *284*, 119762.
[42] X. Deng, P. Chen, X. Wang, R. Cui, C. Deng, *Sci. China Mater.* **2023**, *66*, 2299.
[43] a) W. Yang, L. Zhang, J. Xie, X. Zhang, Q. Liu, T. Yao, S. Wei, Q. Zhang, Y. Xie, *Angew. Chem., Int. Ed.* **2016**, *55*, 6716; b) W. Yang, L. Zhang, J. Xie, X. Zhang, Q. Liu, T. Yao, S. Wei, Q. Zhang, Y. Xie, *Angew. Chem.* **2016**, *128*, 6828.
[44] Q. Lin, Y.-H. Li, M.-Y. Qi, J.-Y. Li, Z.-R. Tang, M. Anpo, Y. M. A. Yamada, Y.-J. Xu, *Appl. Catal., B* **2020**, *271*, 118946.
[45] S. Zhang, Z. Zhang, Y. Si, B. Li, F. Deng, L. Yang, X. Liu, W. Dai, S. Luo, *ACS Nano* **2021**, *15*, 15238.
[46] S. Zhang, X. Liu, C. Liu, S. Luo, L. Wang, T. Cai, Y. Zeng, J. Yuan, W. Dong, Y. Pei, Y. Liu, *ACS Nano* **2018**, *12*, 751.
[47] G. Sun, S. Mao, D. Ma, Y. Zou, Y. Lv, Z. Li, C. He, Y. Cheng, J.-W. Shi, *J. Mater. Chem. A* **2019**, *7*, 15278.
[48] M. Wang, G. Zhang, Z. Guan, J. Yang, Q. Li, *Small* **2021**, *17*, 200695.
[49] X.-L. Li, G.-Q. Yang, S.-S. Li, N. Xiao, N. Li, Y.-Q. Gao, D. Lv, L. Ge, *Chem. Eng. J.* **2020**, *379*, 122350.
[50] C. Du, Q. Zhang, Z. Lin, B. Yan, C. Xia, G. Yang, *Appl. Catal., B* **2019**, *248*, 193.
[51] J. Xie, H. Zhang, S. Li, R. Wang, X. Sun, M. Zhou, J. Zhou, X. W. (D.) Lou, Y. Xie, *Adv. Mater.* **2013**, *25*, 5807.
[52] Y. Li, S. Yu, J. Xiang, F. Zhang, A. Jiang, Y. Duan, C. Tang, Y. Cao, H. Guo, Y. Zhou, *ACS Catal.* **2023**, *13*, 8281.
[53] X. Ye, Y. Chen, C. Ling, J. Zhang, S. Meng, X. Fu, X. Wang, S. Chen, *Chem. Eng. J.* **2018**, *348*, 966.